Journal of Hazardous Materials 458 (2023) 131873

Contents lists available at ScienceDirect

Journal of Hazardous Materials

journal homepage: www.elsevier.com/locate/jhazmat

Engineering boron and nitrogen codoped carbon nanoarchitectures to tailor molecularly imprinted polymers for PFOS determination

Mattia Pierpaoli [a,*], Małgorzata Szopińska [b], Adrian Olejnik [a], Jacek Ryl [c], Sylwia Fudala-Ksiażek [b], Aneta Łuczkiewicz [b], Robert Bogdanowicz [a]

[a] Faculty of Electronics, Telecommunication and Informatics, Gdańsk University of Technology, Poland
[b] Faculty of Civil and Environmental Engineering, Gdańsk University of Technology, Poland
[c] Institute of Nanotechnology and Materials Engineering, Gdańsk University of Technology, Poland

HIGHLIGHTS

- Molecularly imprinted polymer (MIP) has been realized on tailored carbon nanoarchitectures.
- Tailoring the MIP substrate by CVD positively affects PFOS binding constant.
- CNW/MIP PFOS sensor well performed in tap water and treated wastewater.
- The transducer's higher surface area is beneficial to MIP.
- DFT studies suggest the formation of specific C-N bonds between MIP and CNW.

GRAPHICAL ABSTRACT

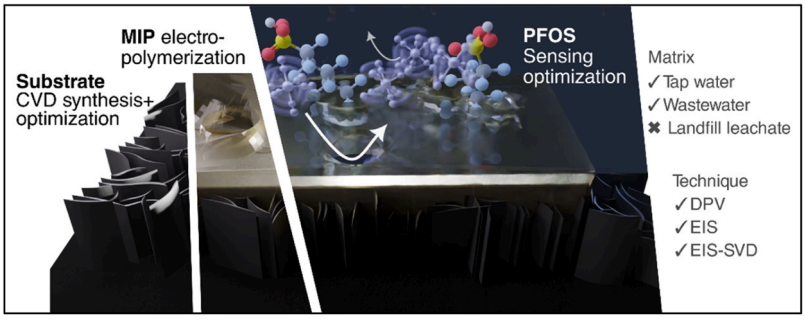

ARTICLE INFO

Editor: <Lingxin CHEN>

Keywords:
MIP
Perfluorooctanesulfonic acid
Carbon nanomaterial
Environmental sensing
Wastewater
Forever chemicals

ABSTRACT

Per- and polyfluoroalkyl substances (PFAS) have gained significant attention as emerging contaminants due to their persistence, abundance, and adverse health effects. Consequently, the urgent need for ubiquitous and effective sensors capable of detecting and quantifying PFAS in complex environmental samples has become a priority. In this study, we present the development of an ultrasensitive molecularly imprinted polymer (MIP) electrochemical sensor tailored by chemically vapour-deposited boron and nitrogen codoped diamond-rich carbon nanoarchitectures for the selective determination of perfluorooctanesulfonic acid (PFOS). This approach allows for a multiscale reduction of MIP heterogeneities, leading to improved selectivity and sensitivity in PFOS detection. Interestingly, the peculiar carbon nanostructures induce a specific distribution of binding sites in the MIPs that exhibit a strong affinity for PFOS. The designed sensors demonstrated a low limit of detection (1.2 μg L^{-1}) and exhibited satisfactory selectivity and stability. To gain further insights into the molecular interactions between diamond-rich carbon surfaces, electropolymerised MIP, and the PFOS analyte, a set of density functional theory (DFT) calculations was performed. Validation of the sensor's performance was carried out by successfully determining PFOS concentrations in real complex samples, such as tap water and treated wastewater, with average recovery rates consistent with UHPLC-MS/MS results. These findings demonstrate the potential of MIP-supported diamond-rich carbon nanoarchitectures for water pollution monitoring, specifically

* Correspondence to: Department of Metrology and Optoelectronics, Faculty of Electronics, Telecommunication and Informatics, Gdańsk University of Technology, Gabriela Narutowicza 11/12, 80–233 Gdańsk, Poland.
E-mail address: mattia.pierpaoli@pg.edu.pl (M. Pierpaoli).

https://doi.org/10.1016/j.jhazmat.2023.131873
Received 27 March 2023; Received in revised form 13 June 2023; Accepted 14 June 2023
Available online 16 June 2023
0304-3894/© 2023 The Authors. Published by Elsevier B.V. This is an open access article under the CC BY-NC-ND license (http://creativecommons.org/licenses/by-nc-nd/4.0/).

targeting emerging contaminants. The proposed sensor design holds promise for the development of in situ PFOS monitoring devices operating under relevant environmental concentrations and conditions.

1. Introduction

Perfluorooctanesulfonate (PFOS) is an anthropogenic compound belonging to the class of persistent pollutants of emerging concern found in water, air, fish and soil at locations around the world and known for its long persistence in the environment, and recently proposed as a CERCLA hazardous substance [14]. In addition, PFOS, together with other per- and polyfluoroalkyl substances (PFAS), are reproductive and developmental toxicants, endocrine disruptors and potential human carcinogens. A recent analysis of impacts from PFAS exposure in Europe and the United States identified health-related costs between tens and hundreds of billions annually, revealing the magnitude of the problem [10]. For these reasons, their occurrence and concentration should also be monitored using ubiquitous and inexpensive monitoring techniques, supported by standard chromatographic reference techniques, as described in the latest European Directive on the quality of water intended for human consumption [58]. Indeed, these techniques can complement traditional analytical techniques such as HPLC-MS/MS, offering a more comprehensive and efficient approach to PFOS monitoring and environmental protection (e.g. increased spatial coverage, real-time monitoring, early warning systems).

The first reported technique for the preparation of molecularly imprinted polymers (MIPs) for detecting PFOS in water dates back to 2018 by the group of Ugo and colleagues [25], by electropolymerizing the sensing layer (eMIP) on gold and reaching a LOD of 0.04 nM. In order to accelerate the analyte mass transfer rate and improve the adsorption performance, it is possible to incorporate nanocomposite adsorbents within the MIP layer [62]. Indeed, different monomers and substrates have been used for the development of MIP-based PFOS sensors, such as carbon-fluorine and quaternary ammonium salt on carbon microspheres [22], and o-phenylenediamine on glassy carbon [9] and gold [25] macroelectrodes. A variety of carbon-based nanostructured materials have been developed and employed in MIPs, ranging from (0D) nanoparticles [57], carbon dots [63], (1D) nanotubes [41], (2D) laser-induced graphene [4] and (3D) boron-doped diamonds [48] as functional supports, providing higher surface area and enhanced charge transfer. B,N-codoped carbon nanowalls (CNWs) are open-boundary, vertically oriented, few-layer graphene sheets with exceptional properties [6] prepared by microwave plasma-enhanced chemical vapour deposition (MPECVD). The MPECVD synthesis duration and gas precursor ratios and compositions can be varied to achieve tailored substrates as MIP transducers. Since the recognition layer is polymerised directly onto the transducer surface in eMIPs, the morphology of the latter directly influences the actual exposed electroactive surface and its chemical composition determines the electrical properties of the eMIP. For these reasons, the choice of electrochemical technique used to convert the electrical signal into the analyte concentration is a key factor. While the MIP sensing layer optimisation has been carried out in the literature in terms of polymer-analyte interaction, both experimentally and by molecular dynamics simulations [11,16], the effect of tailoring the substrate morphology at the micro/nano scale on the MIP performance has not been systematically investigated.

Differential Pulse Voltammetry (DPV) involves superimposing a fixed amplitude pulse on a step potential and measuring the current before and after the pulse. For non-electroactive analytes, such as PFOS, the presence of a redox probe is required to find the Faradaic current by subtraction of the measured currents. Therefore, the deduced concentration is actually the ability of the redox pair to diffuse across the electrode surface. On the other hand, electrochemical impedance spectroscopy (EIS) is based on the application of a small perturbation (on the order of tens of millivolts) over a discrete range of frequencies and does not require the presence of a label. In fact, after fitting the experimental data with an arbitrary electrical equivalent circuit (EEC), it is possible to correlate the change in charge transfer resistance or capacitance caused by changes in the MIP electrode directly with the analyte concentration. In addition, the elimination of the redox couple falls within the 'GREENIFICATION' principles for MIP [39], making the EIS technique preferable. Thus, in a classical quantitative analytical method, changes in the Faradaic current or EEC component characteristics can be directly related to the analyte concentration by simple regression, under the hypothesis that all other interferences have been eliminated or adequately reduced. To overcome these problems, chemometric tools offer a simpler and more straightforward approach to processing whole data without losing valuable information and without the need for supervised interpretation, paving the way for MIP implementation in point-of-care devices. Geladi et al. [20] introduced the use of singular value decomposition (SVD) to analyse of impedance spectra as complex numbers, allowing principal component analysis (PCA) to be performed directly on the original data. Similarly, Rodrigues et al. used an analogous method to obtain quantitative prediction models for hydroquinone and catechol using a carbon nanotube paste electrode [49] and, in our previous study, to directly correlate a raw EIS analysis with the alpha-amino acid concentration [45].

In this study, we demonstrate the significance of optimising the interaction between the substrate and molecularly imprinted polymers (MIPs) by manipulating the nanoscale morphology and chemical composition. For the first time, we engineered B,N-codoped carbon nanowalls (CNWs) to tailor MIP scaffolds for the improved detection of PFOS in real aquatic samples. Our findings showed that the presence of diamond-rich carbon nanostructures induces a specific distribution of binding sites in MIPs that exhibit a strong affinity for PFOS. This aspect is crucial to investigate since MIPs are typically equipped with a wide array of binding sites that vary in their affinities [61]. The introduction of this nanoarchitectured surficial transducer strategy plays a significant role in enhancing the sensitivity and selectivity, both directly and indirectly. Hence, we establish that it is feasible to reduce the MIP heterogeneity by tailoring the morphology and composition of the substrate, thereby enhancing the overall performance of the MIPs. By controlling the properties through MPECVD synthesis, we were able to identify the most influential parameter affecting PFOS detection, and chemometric tools were employed to predict the PFOS concentration and offer valuable insights into the detection mechanism. Moreover, we conducted extended density-functional theory (DFT) simulations to support the experimental outcomes.

2. Materials and methods

2.1. Reagents and materials

Perfluorooctane sulphonic acid potassium salt (PFOS, ≥98.0 %), perfluorodecanoic acid (PFDA, ≥98.1 %), perfluorooctanoic acid (PFOA, ≥99.7 %) and perfluorohexanesulfonic acid (PFHxS, ≥ 99 %) were purchased from Sigma-Aldrich and Dr. Ehrenstorfer™ (LCGC). o-Phenylenediamine (oPD) was purchased from Chemat. Other chemical reagents (e.g., potassium ferrocyanide and ferricyanide, potassium hydrogen phosphate, phosphoric acid, methanol – MeOH) were reagent grade (≥95 %) from Chempur. A 100 mM phosphate solution (PS) was used as the electrolyte (8.7331 g K_2HPO_4 and 125 µL 85 % H_3PO_4 were dissolved in a 500 mL volumetric flask using distilled water). The PFOS stock solution was used to prepare the set of solutions with concentrations of 0.01, 0.02, 0.1, 0.2, 1, 2, 10, 20, 100, 200 µg L^{-1} in distilled water. The set of solutions was then mixed in a 1:1 ratio to spike the

MOST WIEDZY Downloaded from mostwiedzy.pl

different water matrices and used for calibration. Detection was performed using concentrations different from those in the calibration set.

2.2. Substrate preparation

The BDD and CNW substrates were fabricated using a microwave plasma enhanced chemical vapour deposition (MPECVD) system (SEKI Technotron AX5400S, Japan) on 10 × 10 mm p-type silicon wafer slides < 100 > . Prior to deposition, the substrates were subjected to RCA cleaning, ultrasonicated in acetone and isopropanol, rinsed and seeded by ultrasonication in a water-based diamond slurry. The detailed procedure for the BDD and CNW can be found in our previous studies [43, 44]. The microwave power and total pressure were kept constant. The process duration and gas feed ratio were varied to obtain different morphologies of CNW, BDD and their hybrid. The CVD stage temperature was kept at 700 °C and the microwave power at 1300 W. H_2, CH_4, and B_2H_6 were used as precursors for the BDD electrode, while N_2 was introduced for the CNW electrode.

2.3. MIP Synthesis

The MIP electrosynthesis was performed directly on the bare BDD and CNW electrodes as synthesised by MPECVD, without any pretreatment. Cyclic voltammetry was performed in a three-electrode configuration between 0 and 0.8 V vs. Ag/AgCl 3 M KCl at a scan rate of 50 mV s^{-1} for a total of 8 cycles in a 2 mL PS/MeOH (2:1 v/v) solution (pH = 8) containing 1 mM PFOS and 10 mM oPD, unless otherwise stated. A non-imprinted control electrode (NIP) was similarly prepared in the absence of the analyte. Different solutions and conditions were tested for template removal. Finally, after electropolymerisation, the electrode was rinsed with distilled water, then kept in a solution of NaOH/MeOH (1:1 v/v) for 20 min, followed by three washes with distilled water. A schematic representation of the electrode preparation is shown in Fig. 1A.

2.4. Chemical-morphological characterisation

Scanning electron microscopy (SEM) using an FEI Quanta 250 FEG with a 20 kV beam acceleration voltage, operating in high vacuum mode and equipped with a secondary electron detector (SED) was used to investigate the electrode morphology. X-ray photoelectron spectroscopy (XPS) analyses were carried out using a Thermo Fisher Scientific Escalab 250 Xi multispectroscope with an AlKα X-ray source, 500 μm in diameter. A pass energy of 20 eV was used to obtain high resolution spectra. A low-energy electron and Ar+ ion flux was used for charge compensation with a final calibration using adventitious C 1s at 284.6 eV. A Horiba Jobin Yvon LabRAM Aramis Raman spectrometer, equipped with an Olympus BX41 confocal microscope and a Horiba Jobin Yvon Synapse CCD camera was used to collect spectra. Excitation was performed with a 632 nm Melles Griot helium-neon laser. Surface observations were made using a x50 LWD objective, D0 filter, 300 l mm^{-1} grating.

2.5. Electrochemical characterisation

The electrochemical behaviour of the carbon nanostructured electrodes was investigated by differential pulse voltammetry (DPV), cyclic voltammetry (CV) and electrochemical impedance spectroscopy (EIS) using a VMP-300 galvanostat-potentiostat (BioLogic) controlled by the EC-lab software. All electrochemical studies were performed in a three-electrode cell configuration after purging with argon. A platinum wire was used as the counter electrode, while Ag/AgCl/3 M KCl or Ag/AgCl wire was used as the reference one. The diameter of the working electrode was 4 mm. CV measurements were performed on BDD, CNW and BDD/CNW electrodes in 5 mM $K_3[Fe(CN)_6]$ + 5 mM $K_4[Fe(CN)_6]$ in 1 M Na_2SO_4 solution at different scan rates (5, 10, 25, 50, 100, 150, 300 mV s^{-1}). EIS was recorded over the frequency range 0.01 Hz to

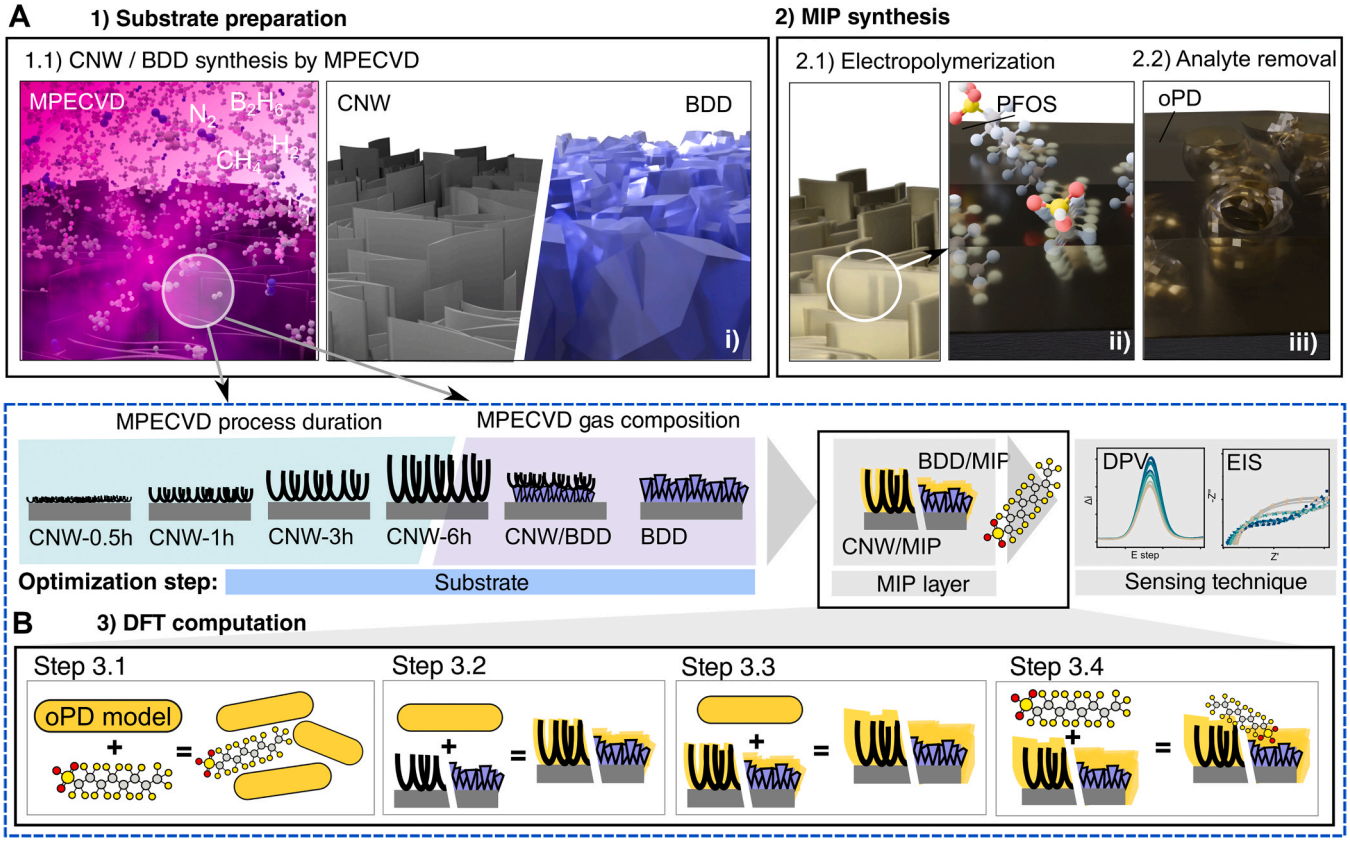

Fig. 1. (A) Schematic representation of the electrode fabrication and detection mechanism. (B) Simulation procedure adopted in this study.

MOST WIEDZY Downloaded from mostwiedzy.pl

100 kHz with a perturbation amplitude of 10 mV. The data were fitted to a modified Randles equivalent circuit (EEC) in which the solution resistance (R_s) is in series with the charge transfer resistance, R_{ct}, and the Warburg W element is in parallel with a constant phase element (CPE) to represent the electrical double layer capacitance due to surface electrical heterogeneity, reactivity distribution and surface porosity and roughness [45]. The effective capacitance of the CPE was calculated using the following equation [6,23]:

$$C_{eff} = Q^{\frac{1}{n}}\left(\frac{R_s R_{CT}}{R_s + R_{CT}}\right)^{\left(\frac{1-\alpha}{\alpha}\right)} \quad (1)$$

The electrochemically active surface area (EASA) was estimated as follows:

$$EASA = \frac{C_{DL}}{C^*} \quad (2)$$

where C_{DL} was obtained from the experimental data and C* is approximately 60 μF (real $cm^2)^{-1}$ for porous materials, regardless of its composition and 25 μF (real $cm^2)^{-1}$ for BDD samples [12].

2.6. Optimised PFOS detection method

2.6.1. PFOS detection in phosphate buffer

The detection of PFOS in 0.1 M PS (pH = 8.05 ± 0.08) was performed by both EIS and DPV methods in the range of 0.005–50 nM. Furthermore, DPV and EIS were performed in PS after 12 min acclimatisation in 2 mL of real environmental samples from tap water (TW), treated wastewater (WW), and landfill leachate (LL) spiked with PFOS. EIS was performed in the frequency range of 100 kHz to 100 mHz, with an amplitude of 10 mV at the formal potential. The DPV parameters were optimised as follows: a scan rate of 13 mV s^{-1}, a pulse height/amplitude of 50 mV, a pulse width of 50 ms and a step height of 10 mV. The potential ranged from 0 V to 0.6 V (vs. Ag/AgCl/3.0 M KCl). All our analyses were performed using duplicate or triplicate samples to ensure the reliability and reproducibility of the results.

2.6.2. PFOS detection in real samples

In this study, the LL sample was collected from the 'Eko Dolina Lezyce' municipal solid waste facility, located in northern Poland [18]. The WW sample was collected from a conventional wastewater treatment plant (WWTP, 470,000 population equivalent), also located in northern Poland. TW was collected from a tap at the Technical University of Gdansk. All samples were taken in June 2022. To determine the concentration of PFOS in the real sample solution, ultra-high performance liquid chromatography coupled with tandem mass spectrometry (UHPLC-MS/MS, Shimadzu Nexera X2; LC MS-8040) was used as a reference method. The EPA 537.1 method was modified and adapted for the purposes of the study. The analytical column used was a Shim-pack SP-C18, 2.1 × 150 mm and 2.7 μm. PFOS was determined by the multiple reaction monitoring (MRM) method in negative ionisation mode with precursor and product ions at 499.00 → 79.95 (m/z). A single-point calibration procedure was used. No analyte preconcentration was applied.

2.6.3. Multivariate data analysis

The matrix **Z** is given by the total impedance, expressed in the form of $Z = Z' + jZ''$, where Z' and Z'' are the real and imaginary parts of Z, respectively, and $j^2 = -1$, for each test at a given concentration. Singular value decomposition (SVD) is then applied directly to **Z** to both obtain the left unitary (**U**) and right conjugate transpose (**V***) matrices, where:

$$\boldsymbol{Z} = \mathbf{U}\boldsymbol{\Sigma}\mathbf{V}^* \quad (3)$$

The calibration curve is then realised by finding the least square solution $\mathbf{Zx} = \mathbf{b}$, where b is the concentration-containing vector, by truncated-SVD, according to:

$$\widetilde{\mathbf{x}} = \widetilde{\mathbf{V}}\widetilde{\boldsymbol{\Sigma}}^{-1}\widetilde{\mathbf{U}}^*\mathbf{b} \quad (4)$$

The SVD calculations were performed in the R software and environment [47].

2.7. Density functional theory (DFT) computations

Molecular structures of the PFOS molecules, oPD polymer models and surface slabs were built in the Atomistix ToolKit enviornment (Atomistix Toolkit Version 2019.03, Synopsys QuantumWise, USA) environment. Density functional theory (DFT) computations were performed using the Perdew–Burke–Ernzerhof (PBE) functional within the generalised gradient approximation (GGA) as implemented in the package. The Linear Combination of Atomic Orbitals (LCAO) method [56] with double-zeta polarised ATK basis set and FHI norm-conserving pseudopotentials were applied [59]. The Brillouin zone was sampled according to the Monkhorst-Pack grid of 4 × 4 × 1 for slabs with periodic boundary conditions and multipole boundary conditions for isolated molecules. Geometry optimisations were performed with a 0.05 eV/Ang force cutoff. Electron density maps and electrostatic potential maps were plotted using the default tools implemented in the ATK package. All the simulation steps are pictured in Fig. 1B.

The first step of the simulations was establishing the oPD polymer model and investigating the interactions between the PFOS molecule and those polymer models with different molar ratios – 1:1, 1:2, 1:3 and 1:4 – and different geometric configurations. Such ratios were applied in a similar DFT coupled with experiment studies [26,30,35].

The second step consisted of adsorption of the oPD polymer model (trimer) on the slabs reflecting the surfaces of the carbon-based electrodes used in the experiments. In those adsorption simulations, trimer molecules were placed above the slab (several Ang) with a 0.05 eV/Ang force tolerance, where the four topmost carbon layers were allowed to relax, and all deeper layers were fixed. This methodology has been described thoroughly in our recent work [38]. Such adsorption calculations were performed for three types of surfaces – diamond (220), flat graphite (0002) and vertically oriented graphite (11−20). In general, diamond (220) slabs are models of the BDD electrode and the mixture of all three slabs can be viewed as the model of the real BCNW.

The third step involved adsorbing the second layer of the MIP on the slab already containing the first layer – thus modelling the growth of the MIP. The obtained structure was relaxed analogously with the same constraint on the bottom pieces of the slab, but without constraints on the first MIP layer. The optimised structure of the two-layered MIP is intended to serve as a model for the plastic cavity for the PFOS analyte – details are elaborated in the results section.

In the fourth and the last step, the PFOS molecule was placed inside the cavity formed on three surfaces. Interaction energies were calculated for all three modified surfaces, and all formed covalent and non-covalent bonds were analysed by visual inspection, electron density maps and electrostatic potential difference maps. Binding/interaction/adsorption energies were calculated according to the standard formula:

$$E_{binding} = E_{complex} - E_{isolated\ constituents}$$

where the complex and isolated constituents vary depending on the simulation conditions described within the text and in the Figures. Additional details are reported in the Supplementary information.

3. Results and discussion

3.1. Sensor morphological and molecular characterisation

Micrographs of the as-grown substrate surfaces are shown in Fig. 2A–F. The differences between the polycrystalline boron doped diamond electrode (Fig. 2A) and the CNW substrates are readily

MOST WIEDZY Downloaded from mostwiedzy.pl

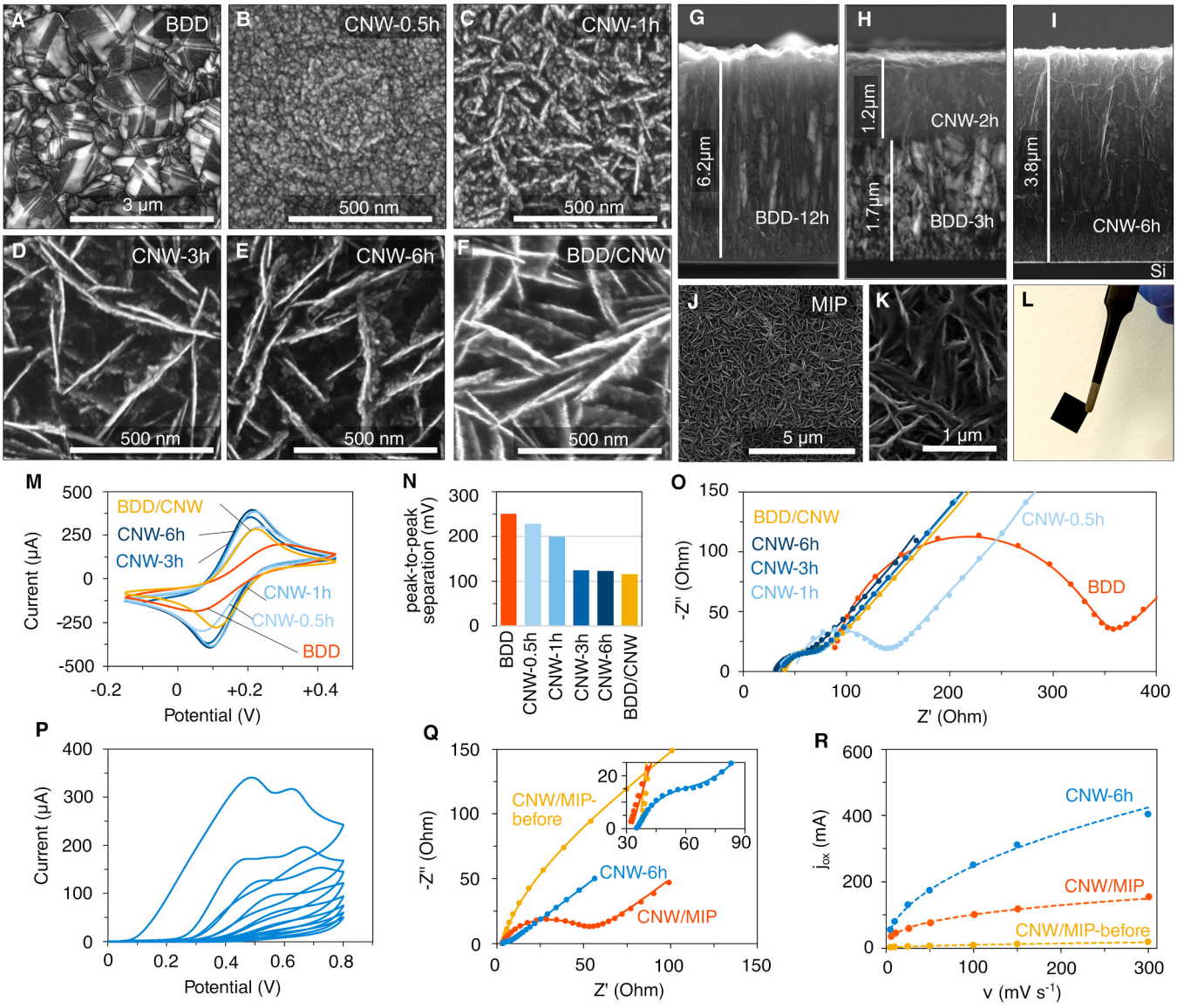

Fig. 2. (A) Bare BDD, (B–E) CNW, (F) BDD/CNW SEM top view. Cross section of (G) BDD, (H) BDD/CNW and (I) CNW-6 h samples. (J) Top view of the MCNW-6 h/MIP electrode, (K) its magnification, and (L) its photograph. (M) Voltammogram in 1 M Na_2SO_4 + 5 mM $[Fe(CN)]_6^{3-/4-}$ redox couple, (N) peak-to-peak separation, and (O) Nyquist plots for the bare CNW and BDD substrates. (P) Electropolymerisation of oPD on CNW-6 h, (Q) and EIS comparison between the bare, oPD-electropolymerised before and after (MIP) extraction of the analyte. (R) Non-linear fitting of the current-scan rate dependence.

apparent at first glance. In addition, CNW-0.5 h (Fig. 2B) has an irregular surface characterised by small protuberances in the nanometre range. After 1 h of growth time, densely packed wall-like structures had formed (Fig. 2C). With increasing growth time (greater than 1 h), the CNW morphology resulted in well-developed structures with increased spacing (Fig. 2D,E). The SEM of the BDD/CNW (Fig. 2F) sample shows a similar surface morphology to the BDD-6 h. Cross-sections of the grown substrate transducer are shown in Fig. 2G–I for the BDD, BDD/CNW and CNW-6 h samples. The estimated growth rate was approximately 500 nm h^{-1} for the BDD and 610 nm h^{-1} for the CNW layers. The top view of the CNW-6 h after electropolymerisation is reported in Fig. 2J,K, together with its photograph (Fig. 2L).

3.2. Sensor electrochemical characterisation

Investigations of the processes occurring at the electrode/electrolyte interface were carried out by cyclic voltammetry measurements in a 0.1 M Na_2SO_4 solution containing 5 mM ferrocyanide redox couple. CV curves for pristine CNW electrodes are shown in Fig. 2M. It can be observed that the highest peak-to-peak separation belongs to the BDD, while it decreases for the CNW with increasing layer thickness, reaching its asymptotic minimum (124 ± 1 mV) for an MPECVD growth longer than 1 h (Fig. 2N). Interestingly, the BDD/CNW hybrid electrode shows the lowest value, corresponding to 116 mV. A modified Randles model was used to fit the EIS results (Fig. 2O). R_{ct} decreases with the increasing layer thickness, while C_{eff} increases, and thus their capacitive behaviour (Table S1). The voltammogram during the electropolymerisation of oPD on the CNW-6 h sample is shown in Fig. 2P. EIS measurements were performed in the same solution using the bare and MIP-coated CNW-6 h electrode before and after PFOS extraction and presented as Nyquist plots in Fig. 2Q with the inset showing the magnification for the high frequency region. The semicircles of the Nyquist plots were fitted using the same modified Randles EEC and the results are reported in Tables S2. Fig. 2R shows the anodic current peak at different scan rates for the different samples. After the deposition of o-PD on the CNW surface, a significant loss of redox peak response was observed (Fig. S1B) compared to the bare surface (Fig. S1A), indicating a uniform surface coverage. After the removal of the analyte, part of the substrate surface

MOST WIEDZY Downloaded from mostwiedzy.pl

became newly available to the electrolyte and the redox couple, as shown in Fig. S1C. However, it is interesting to note the presence of a slightly higher rate for the cathodic branch, as also shown by other authors using this particular polymer/redox probe combination [8]. In fact, this aspect may be due to the 'gate effect', due to charge accumulation in the MIP film [53]; the negatively charged $[Fe(CN)_6]^{4-}$/$[Fe(CN)_6]^{3-}$ probe may first bind with the positively charged amine groups ($-NH_3^+$) of the o-PD layer, resulting in an initial depletion of the $[Fe(CN)_6]^{4-}$. In addition, the scan rate shows that the oxidation peak current varies linearly with $\nu^{1/2}$, indicating that it is a diffusion-controlled process, even for the MIP sample, at the lowest measured frequencies (Fig. S1D-F).

The Raman spectra in Fig. 3A suggests that the electropolymerised oPD spectra after 10 cycles of CV is similar to its trimer form [52]. The main bands for the polymerised samples are observed at 998 cm^{-1} cm, related to out-of-plane C–H bending [55] and at 1595 cm^{-1}, due to C=C stretching in a quinonoid ring [1]. Moreover, the peak at 617 cm^{-1} can be recognised, related to in-plane benzene ring deformation [55], while the bands at 1273 cm^{-1} and 1445 cm^{-1} may be associated with the C-N and C=N stretching mode [52,64]. In Fig. 3C, the EDX analysis is reported over a 600 μm segment intersecting the boundary between the functionalised (MIP) surface and the bare CNW surface (Fig. 3B). A clear increase in nitrogen can be observed, due to the successfully polymerised oPD. Moreover, we investigated if the functional groups of the as-grown substrate may play a role in the MIP electropolymerisation process, by preparing an oxidised CNW-6 h sample (o-CNW) by cycling it between 0 and + 0.8 V in PBS, prior to the o-PD electropolymerisation.

The Raman spectra of the bare substrates show the main characteristic D and G peaks at (1333 ± 4) cm^{-1} and (1589 ± 4) cm^{-1}, respectively, together with the two shoulder peaks, D' and D'', due to the CNW [42]. The D band is due to structural edge defects and dangling sp^2 carbon bonds, while the G peak is due to in-plane stretching of sp^2 carbon atoms. For the BDD sample, the characteristic diamond peak is dominant and visible, together with the G peak (Fig. 3D). After both electropolymerisation and simple surface oxidation (o-CNW), the G peak was downshifted compared to the substrate ones, which increased with thicker BCNW substrates, indicating their strong interaction [28]. Moreover, while the shoulder peak D* is generally attributed to the trans-acetylene in bare CVD samples, being more prominent with the increasing synthesis time, its increase in intensity before and after oPD electropolymerisation could be due to the overlapping of C-N stretching. The XPS spectra (Fig. 3E) show that the CNW, o-CNW and BDD surfaces contain mainly oxygen and carbon functional groups, while the MIP and NIP contain additional nitrogen. For the bare CNW samples, the incorporation of boron is observed (Table S3), together with the predominant presence of sp^2 CC bonds (41 % vs. 12 %, Fig. 3F). Moreover, a peak at 284.1 eV was found for the BDD sample, which is a common position for carbon atoms of the diamond lattice present in highly boron doped polycrystalline diamond films. On the other hand, for the MIP and NIP samples, an increase in sp^3 carbon and the presence of amines is directly related to the oPD polymerisation (Fig. 3G).

3.3. PFOS detection mechanism

PFAS are a group of compounds that are difficult to measure directly because they are not electrochemically active. The main difference between faradic and non-faradic electrochemical sensing is the mechanism by which ionic activity is measured, with faradic sensing relying on redox reactions and non-faradic sensing relying on changes in ionic

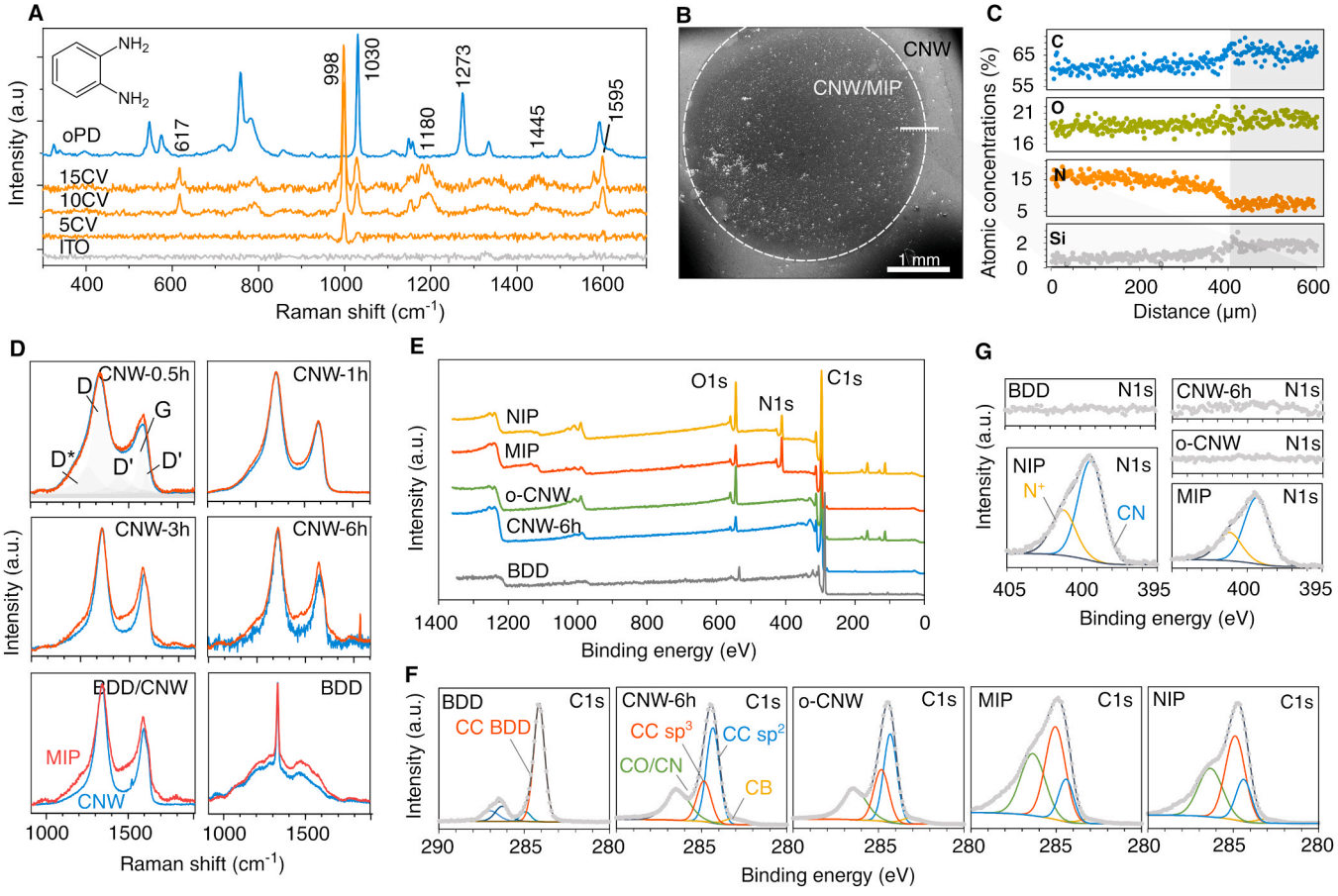

Fig. 3. (A) Raman spectra of oPD and polymerised oPD on ITO at different cycles of CV. (C) EDX along the segment intersecting the MIP boundary (B) with the bare CNW. (D) Raman and (E) XPS spectra of BDD, CNW-6 h, oxidised CNW-6 h (o-CNW), MIP and NIP. Deconvolution of (F) C1s and (G) N1s peaks.

MOST WIEDZY Downloaded from mostwiedzy.pl

conductivity due to MIP cavity depletion.

3.3.1. Faradaic detection of PFOS

As shown in Fig. 4A, the oxidation peak has its maximum in a blank solution, due to the easier accessibility of the CNW surface to the redox probe, while a decrease of the oxidation peak is observed with the increasing concentration. When the current difference is plotted as a function of the PFOS concentration, a non-linear relationship is obtained. The correlation between the peak current measured by DPV and the analyte concentration in PB was fitted by an adaptation of the Langmuir-Freundlich (LF) isotherm, which describes the adsorption of a molecule at different binding sites in heterogeneous systems, with three fitting coefficients [2]. The LF isotherm equation is given below:

$$(i - i_0) = \frac{i_t K C^n}{1 + K C^n} \quad (5)$$

where i_t is related to the maximum number of MIP cavities available, expressed as the peak current limit; K is the Langmuir-Freundlich constant related to the mean binding affinity, and n is the heterogeneity index, which varies from 0 to 1 for physical adsorption. When n = 1, the LF isotherm is reduced to the Langmuir isotherm, while for a heterogeneous material, n < 1. Otherwise, as either C or K approaches 0, the LF isotherm reduces to the Freundlich isotherm. For this reason, the LF model has the advantage of easily accounting for and estimating heterogeneity in the binding behaviour of MIPs. The fitting results and plots are shown in Fig. S2 and Fig. S3. A negligible response was found for the reference CNW/NIP (Fig. S4).

As shown in Fig. 4B, it is interesting to note that the MIP heterogeneity is directly related to the substrate morphology and decreases with the increasing CNW layer thickness. Indeed, the BDD substrate has one of the lowest heterogeneity index, while for the BDD/CNW substrate, only the thickness of the overlying CNW layer is relevant for the MIP sensing activity for the EASA (Fig. 4C). K is known to depend on several parameters, including the surface area and nature of the adsorbent and adsorbate. Therefore, for the CNW samples, K increases with the increasing EASA, while for the BDD substrate, the higher value of K can be attributed to a higher strength of interaction between the BDD surface and the analyte (probably due to the low hydrophilicity induced by the low amount of polar C-N bonds [3] and sp^2-C, rather than the comparable amount of carboxyl and hydroxyl groups [13]. A fortiori, it is possible to observe how the change in the number of binding sites (i_t) relates to the peak current measured in the absence of the analyte, confirming the fact that the distribution of MIP cavities is directly proportional to the available substrate surface (Fig. 4D).

3.3.2. Non-faradaic detection of PFOS

The impedance spectra obtained from the EIS technique were modelled using the EEC described above. The value of R_{CT} showed the biggest change in the EEC elemental characteristics with the increasing PFOS concentration (Fig. 4E), which can be attributed to increased inhibition of change transfer due to the PFOS blocking activity in the MIP cavities. In fact, the diameter of the typical semicircle reported in the Nyquist plot increases with the increasing PFOS concentration. Therefore, a conventional strategy is to plot the change in R_{CT} against the PFOS concentration:

$$(R_{CT} - R_{CT0}) = \frac{R_t K C^n}{1 + K C^n} \quad (6)$$

Interestingly, a similar trend for the n, K and R_{CT} values is observed for the analogous faradaic counterparts. Whereas for both the DPV- and EIS-derived LF isotherms, K increases with the increasing CNW thickness, with the BDD sample showing the highest interaction (Fig. 4G), for R_t analogously, n decreases monotonically with the CNW thickness (Fig. 4F). As counterintuitive as this may seem, the reason is that unlike the DPV-based isotherm, which represents the accessibility of the iron/ferricyanide molecule through the MIP pores, the EIS-based isotherm in this case takes into account the charge transfer resistance associated with the MIP layer. Indeed, the lower R_{ct} corresponds to a lower R_t (Fig. 4H) and the linear relationship is maintained.

3.3.3. PFOS quantification by chemometric approach

Potential pitfalls of classical EIS fitting to the EEC are the

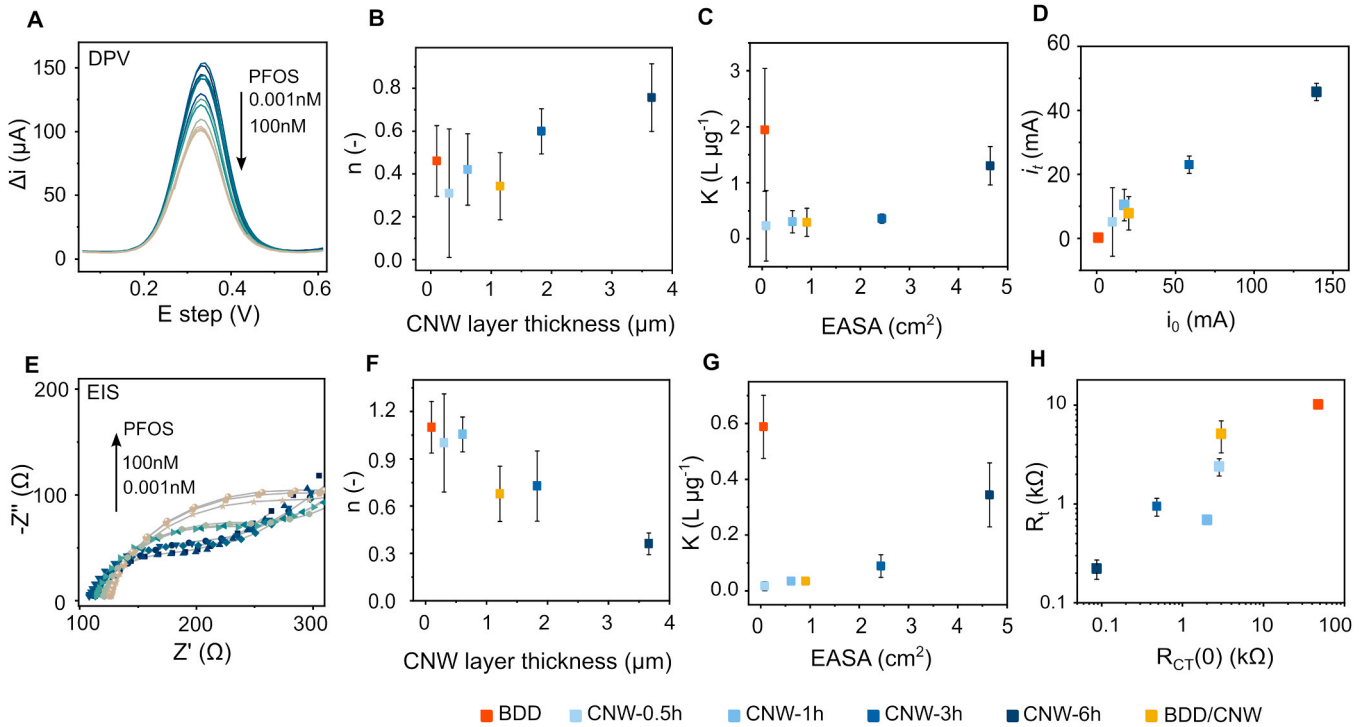

Fig. 4. (A) DPV and (E) EIS for CNW6h/MIP in PS at concentrations of 0.001–100 nM, (B-D) LF coefficients obtained by fitting DPV results to Eq. 3 and (F-H) obtained by fitting EIS to Eq. 4.

MOST WIEDZY Downloaded from mostwiedzy.pl

arbitrariness of the choice of a specific EEC and the possible loss of information from relaxation processes not included in the EEC [21]. For these reasons, applying multivariate data analysis techniques directly to the raw impedimetric measurements can provide useful insights. The CNW-6 h/MIP sample was used as the reference. As the columns are ordered by importance, the first one accounts for more than 98 % of the total variance, and by plotting the real versus the imaginary part of u_1 (Fig. 5A), it can be seen that it resembles the characteristic shape of a Nyquist plot. On the other hand, v_1, the first column of V, discriminates well between the different tests by increasing the PFOS concentration (Fig. 5B). The results of the linear regression performed by SVD are shown in Fig. 5C, where the predicted concentrations are plotted against the measured concentrations after log-transformation. The "pseudo--Nyquist" obtained was then transformed into a "pseudo-Bode" (Fig. 5D) for ease of comparison. By performing linear least squares regression using the t-SVD and PFOS concentration as the column space, the factors were plotted against the frequency (Fig. 5D, in blue) to highlight the intervals most related to the changes in concentration of PFOS. It was observed that the major changes occur mainly at intermediate frequencies (≈20 Hz) for the CNW-6 h/MIP, which is consistent with the observed increase in R_{ct}, becoming the preferred current path at low frequencies (Fig. 5E).

On the other hand, by comparing $\tilde{x}$ as a function of the frequency for the different samples, it can be noticed that the frequency range that has the greatest weight on the linear regression, thus mostly related to the PFOS concentration, decreases with the decreasing CNW thickness (Fig. 5F). In the light of the above considerations, the CNW-6 h substrate transducer was selected for further analysis in real media.

3.3.4. *DFT study*

In Fig. S5A, an electrostatic potential difference map for the PFOS is shown. In general, the sulphonate group is negatively charged with the strongly acidic hydrogen atom. Because of that acidity, it is abstracted in the neutral pH where the detection experiment happens. On the other hand, the alkyl chain of the PFOS is isotopically covered by a cloud of positive electrostatic potential with slightly negative anisotropic regions around the fluorine atoms. Such electrostatic conditions strongly suggest that the initial phase of the molecular recognition would proceed via the sulphonate group and would be facilitated by the positively charged areas of the MIP cavity. An oxidated trimer of the oPD with 'open' conformation has been chosen as the model of the MIP for several reasons. Firstly, it was found that just the dimer is sufficient to replicate most of the electronic and optical properties of the MIP [32]. Although there is variability with respect to the chain size, it is less relevant compared to the oxidation state of the subunits (the issue of an 'open' versus 'closed' structure) [60]. Experimentally, both dimers, trimer and tetramers have been detected using detailed NMR-MS measurements with an increasing content of trimers and tetramers in a neutral synthesis pH [31]. Other works also report that an 'open' benzoimide-like structure of the chain is preferred in a neutral pH, while a 'closed' phenazine-like structure is obtained during acidic synthesis [40]. Moreover, in the case of the oPD electropolymerised in a neutral pH – which is mostly not electroactive [50] – short chains should be dominant [65], however the data are not consistent in this matter [52].

Detailed analyses of the electropolymerisation mechanisms and structure-property relations of the MIP have been performed elsewhere [7,50] and are not the subject of the following calculations. However, in the following discussion, focus will be placed on interactions of the MIP with both the underlying substrate and the PFOS analyte. Therefore, application of the trimer model seems to be a rational compromise between accuracy and time efficiency and is sustained by the Raman analysis.

The electrostatic difference potential map of the trimer is shown in Fig. S5B. It can be clearly seen that the molecule is mostly negatively charged except for the positive, acidic hydrogen atoms of the -NH_2 amine groups in the core of the chain and at the terminal -NH group. As the real MIP is a collection of oPD chains stacked together, interactions between trimers were also simulated (Fig. S5C,D). Two cases (two minima on the potential energy surface) were considered – the configuration with exactly parallel molecules (subfigure C) and one where the

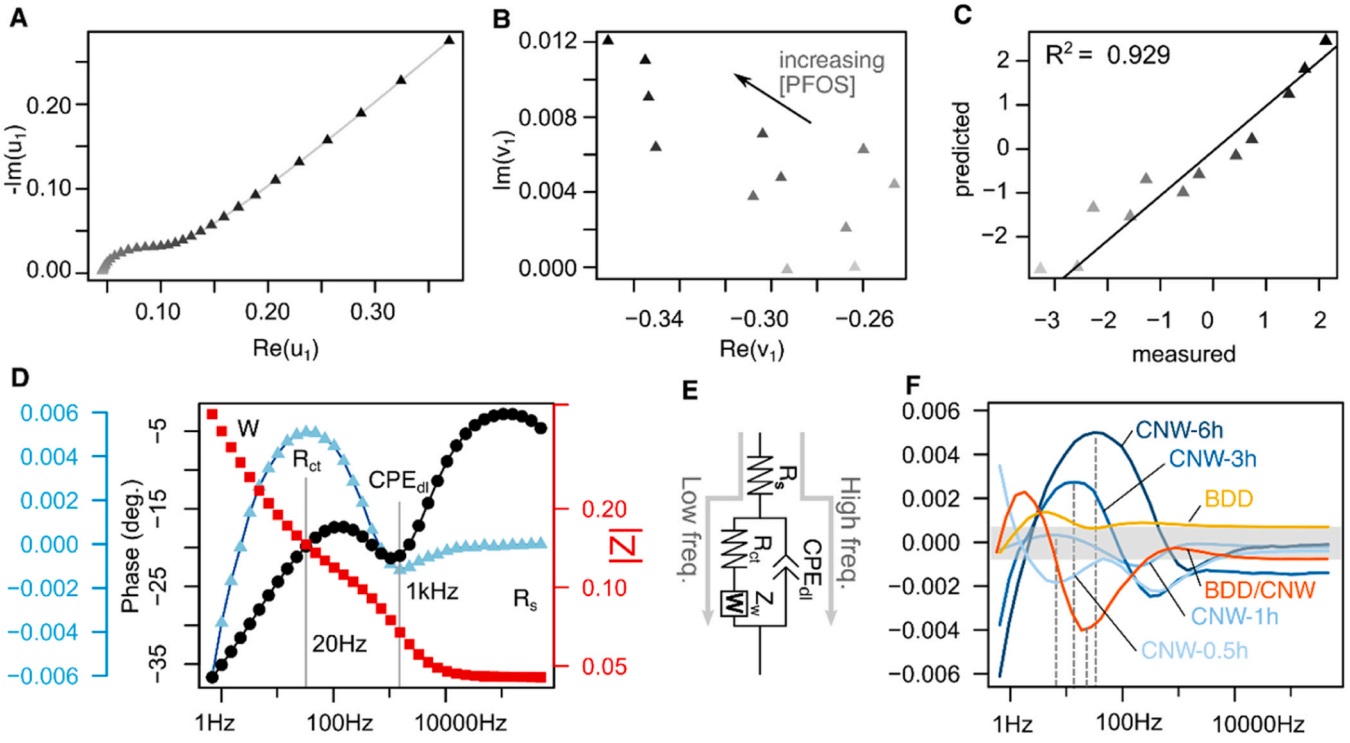

Fig. 5. (A) Nyquist plot of u_1, (B) plot of v_1, (C) comparison between the measured and predicted values by PLS-regression performed by SVD, for CNW-6 h/MIP. (D) Bode plot with $\tilde{x}$ (blue). (E) schematic of the EEC used, and (F) comparison of $\tilde{x}$ for the different substrates synthesised.

MOST WIEDZY Downloaded from mostwiedzy.pl

chains are twisted by a 60° angle with respect to each other (subfigure D). Interestingly, both setups exhibit a similar binding energy, equal to − 0.62 and − 0.63 eV, respectively, evidencing that assembly of the chains should be thermodynamically spontaneous. Moreover, those two configurations are presumably equally probable to occur in the full polymer and can switch between each other due to thermal motions. Electron density maps plotted with a 0.1 eV/Ang^3 cutoff strongly suggest the non-covalent character of the assembly, which will be further relevant after the adsorption on different electrodes.

Additionally, interactions of PFOS with the MIP models were investigated. The optimal configurations with corresponding electron density maps are shown in Figs. S5E-H for single trimers and in Figs. S5I-K for double, triple and quadruple interactions. The T-shaped interaction can be considered as an initial 'approach' phase of the molecular recognition. It is evidenced that the binding of the sulphonate group towards the rings of the MIP (equal to −0.05 eV) is stronger than the binding of the CF_3 group at the other end of the molecule (equal to +0.16 eV). In fact, the positive value of the second indicates that such interaction is thermodynamically unfavourable and non-spontaneous.

Subsequently, the PFOS molecule is likely to bind further to the MIP via its fluorinated alkyl chain. Two possibilities have been considered (subfigures G–H), either through the C-F—N bond with a nitrogen atom bridging two oPD monomers, or the C-F—π bond with the middle subunit of the trimer. The corresponding binding energies are equal to − 0.15 eV and − 0.36 eV. Surprisingly, it is the C-F—π interaction that provides stronger binding and closer contact between the molecules accompanied by a higher electron density overlap. Although all investigated interactions are necessarily non-covalent, the C-F—π bond seems to be crucial for the binding of this particular analyte. The same picture is preserved when several trimer molecules approach the PFOS, further reducing the free energy of the system (the values are reported in Table 1). Interestingly, the more molecules cloak the PFOS chain, the higher the electron density overlap that can be observed visually (subfigures I–K). In other words, a higher density of MIP molecules on the sensor surface should result in a higher binding affinity of the PFOS. Of course, this statement is just a heuristic because, in the real experiment, steric hindrance effects can cause the opposite effect when the layer is too compact.

After establishing interactions between components of the MIP coating, the influence of the substrate material on the MIP conformation was studied. The BDD electrode was modelled as a diamond slab cleaved along the (220) plane with 1% boron doping in the subsurface layers. It has been shown that this crystallographic plane is abundant across different types of BDD [15]. CNW, on the other hand, can be considered a mixture of plain graphite (0002) and vertical graphite (11−20) sheets – such results have been obtained using precise TEM imaging of nanowalls [5]. Therefore, both of those two surfaces were chosen for DFT modelling, representing presumably different microscopic areas of the same CNW material.

Interactions of the single trimer with the abovementioned surfaces are depicted in Figs. S6A-C with electron density maps. In the case of the BDD, it can be seen that one of the rings in the polymer is parallel to the plain, while the other two have phenyl-phenyl dihedrals equal to roughly 45 and 90 degrees. No covalent interactions and significant electron density overlaps were detected, suggesting purely electrostatic/vdW physisorption on the BDD accompanied with the lowest adsorption energy equal to − 2.04 eV (see Table 2). An analogous trend can be observed in the case of flat graphite, although phenyl rings attain a slightly more 'parallel' conformation (smaller values of dihedrals) due to the vdW attraction induced by the graphite sheets. This, in turn, enhances the binding of the trimer slightly (−2.15 eV). On the other hand, there is a clear covalent bonding of the MIP to the vertical graphite through the specific C-N bond with the terminal amine groups of the trimer (1.40 Ang length). Such configuration implies the strongest binding of the MIP (−3.28 eV) to the surface and imposes the rigidity of the first MIP layer. Those effects are presumably associated with the higher homogeneity of the real MIP on the CNW electrode in contrast to the BDD.

Fig. 6A–C depict the optimised geometry of the second MIP layer reflecting the growth of the MIP. In general, assembly is expected to be thermodynamically spontaneous on all the surfaces and most favourable on the flat graphite (−1.94 eV compared to −1.13 eV and −1.14 eV). This feasibility of the flat graphite can be explained by the electrostatic/vdW drive for the trimer to attain a flat conformation – where the vdW attraction is maximised. Additionally, supercell multiples of the two-layered MIP models are shown in the top-view in Figs. S6D-F with electrostatic potential maps. The main purpose of this step is to estimate the most favourable positions of the PFOS molecule placement in such a system. Knowing the sulphonate group is negatively charged in a neutral pH (Fig. S5A) and assuming the initial step of recognition is realised via these groups (Fig. S5E), the positive areas on the surface should be optimal. These areas can be found at all surfaces generated in the vicinity of MIP molecules, even though the trimer molecules themselves are surrounded by a negative charge. Fortunately, the positive and negative areas are well-separated in the space, which has been found to be beneficial for effective sensing [51]. The highest positive potential is observed on the BDD electrodes up to + 2 V compared to + 1 V on the other two. In general, a higher electrostatic potential should lead to more effective weak electrostatic bond formation such as hydrogen bonds [34]. Although interactions different from hydrogen bonds are expected in the case of PFOS, it is expected the BDD surface would exhibit higher binding affinity. It is to be noted that this methodology provides just an estimation of the optimal environment of the template-MIP. In general, a more thorough investigation of the geometry would be required, involving multi-scale approaches, e.g., molecular docking [33,36] or a statistical analysis of the possible conformations [51,54]. However, as the focus of the work is to elucidate the influence of the substrate, not the template-MIP interactions themselves, such a simplified route is justified.

Lastly, PFOS molecules were placed in cavities estimated by the electrostatic potential maps and the structure was relaxed again – all three surfaces are depicted in Fig. 6D-I from side and top perspectives. The corresponding binding energies are given in Table 2. As speculated earlier, the BDD-MIP binds the PFOS with the highest affinity (−1.91 eV) compared to the other two surfaces (−1.05 eV for flat and −1.30 eV for vertical graphite). This energy contains both the interaction of the PFOS with the MIP and the surface. Although some works

Table 1
Free binding energies for trimer-trimer, PFOS–single trimer and PFOS–multiple trimer interactions.

Configurations	Binding free energy [eV]
Trimer-Trimer	
Parallel trimers	−0.62
Twisted trimers (60 deg)	−0.63
PFOS – Single trimer	
T-shaped connection via CF3	+0.16
T-shaped connection via SO3	−0.05
Alkyl – ring via Nitrogen	−0.15
Alkyl – ring via π-π	−0.36
PFOS – Multiple Trimers	
Double	−1.99 (−0.99 per trimer)
Triple	−3.73 (−1.24 per trimer)
Quadruple	−4.63 (−1.16 per trimer)

Table 2
Adsorption free energies of the first MIP layer, second MIP layer and PFOS binding on the BDD (220), flat graphite (0002) and vertical graphite (11–20).

Free energies for [eV]	BDD	Flat graphite	Vertical graphite
First layer adsorption	−2.04	−2.15	−3.28
Second layer adsorption	−1.13	−1.94	−1.14
PFOS binding to the cavity	−1.91	−1.05	−1.30

MOST WIEDZY Downloaded from mostwiedzy.pl

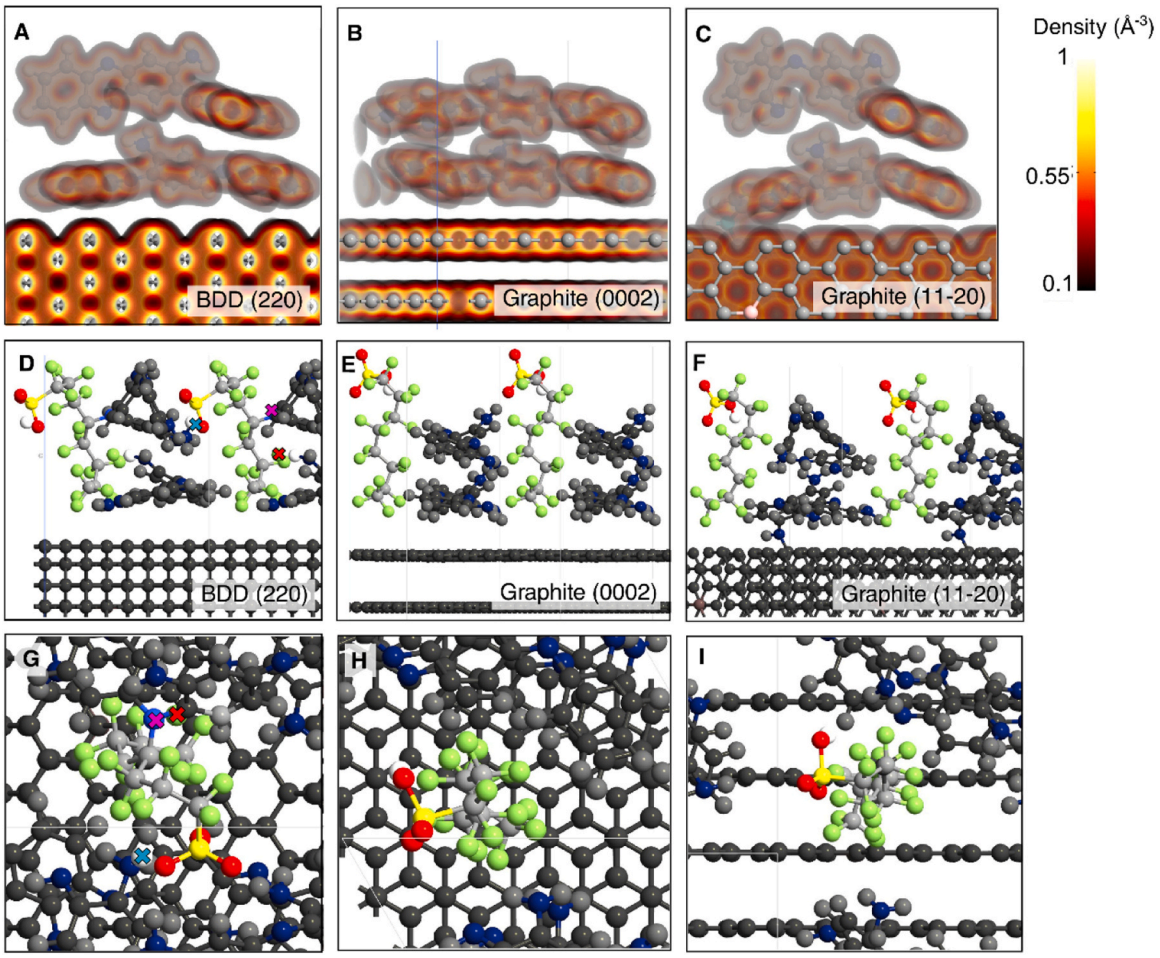

Fig. 6. Molecular structure and interactions of oPD trimers with different electrode models. A-C electron density maps illustrating adsorption of the second MIP layer on the BDD (220), flat graphite (0002) and vertical graphite (11−20); D–F two periodic repetitions of the cell containing PFOS inside the cavity formed on the corresponding surfaces; G–I top-views of the corresponding cavities magnifying interactions between PFOS and the MIP. All atoms except the PFOS constituents are dimmed for clarity. Coloured 'X's in subFigs. D and G correspond to the non-covalent interactions between the PFOS and MIP: N-H—O-S hydrogen bond (turquoise), atypical C-N bond (purple) with 1.41 Ang length, atypical C-F—H-N interaction (red) with fluorine atom slightly abstracted from the alkyl chain (2.13 Ang C-F bond length).

report that the interaction of the analyte with surface can be detrimental to the sensor function [27], in the following case, it is only marginal (less than a 10% contribution). This stands in perfect agreement with the experimental results and K constants obtained via fitting to the Langmuir-Freundlich isotherms. Moreover, in the case of the graphitic models, PFOS-MIP interactions include only non-covalent C-F—π, C-F—H-N and C-F—N interactions. Indeed, there are numerous works showing the strong importance of the hydrogen bond network in the selective recognition and binding intensity [17,36]. There are, however, three stronger bonds detected in the case of BDD-MIP, responsible for stronger binding. These are marked with coloured 'X's in Fig. 6D,G and are attributed to: N-H—O-S hydrogen bond (turquoise), atypical C-N bond (purple) with 1.41 Ang length, atypical C-F—H-N interaction (red) with fluorine atom slightly abstracted from the alkyl chain (2.13 Ang C-F bond length). These three are specific to the BDD-MIP and increase the compactness of the MIP layer associated with higher binding affinity towards PFOS. It is to be noted that all calculations are performed on the PBE level of theory, which is not an optimal functional for the detailed analysis of novel types of bonds. However, its use is necessary for such a huge molecular system in concert with surface and periodic boundary conditions. Therefore, such interactions observed at the modified BDD surface require more thorough research to be further confirmed in similar systems. Nevertheless, the comparison of those three surfaces shows without a doubt that there is a strong impact of the surface on the conformation of the MIP, which consequently influences the binding capability and molecular interactions with the analyte – in this case, PFOS.

3.4. PFOS detection in real media

Results of the CNW/MIP calibration in real water matrices are reported in Fig. 7A-C.

For both TW and WW, at PFOS concentrations of 10 and 50 ng L^{-1}, no changes are detected, while at increasing concentrations (greater than 0.1 μg L^{-1}), a decrease in the oxidation peak is observed. By plotting both the current and the electrical resistance differences (Figs. S7A-C) as a function of the PFOS concentration, non-linear relationships can be observed that can be fitted with the LF isotherm, except for the LL matrix. Furthermore, a good correlation between the measured and predicted values can be observed, but only for the TW and WW matrices, by linear regression using SVD and Eq. 4 (Fig. S7D-F). The inability to measure PFOS in LL can probably be attributed to the inhibitory effect of sulphates, where the concentration can reach e.g. 1106 ± 129 mg L^{-1} [46], and humic substances [9]. Table S4 shows the ability of the CNW/MIP sensor to quantify PFOS in TW and WW by spiking real samples with PFOS at different concentrations and comparing the results obtained by the UHPLC-MS/MS technique. The use of the LF isotherm provides an advantage in terms of a higher recovery rate, even over

MOST WIEDZY Downloaded from mostwiedzy.pl

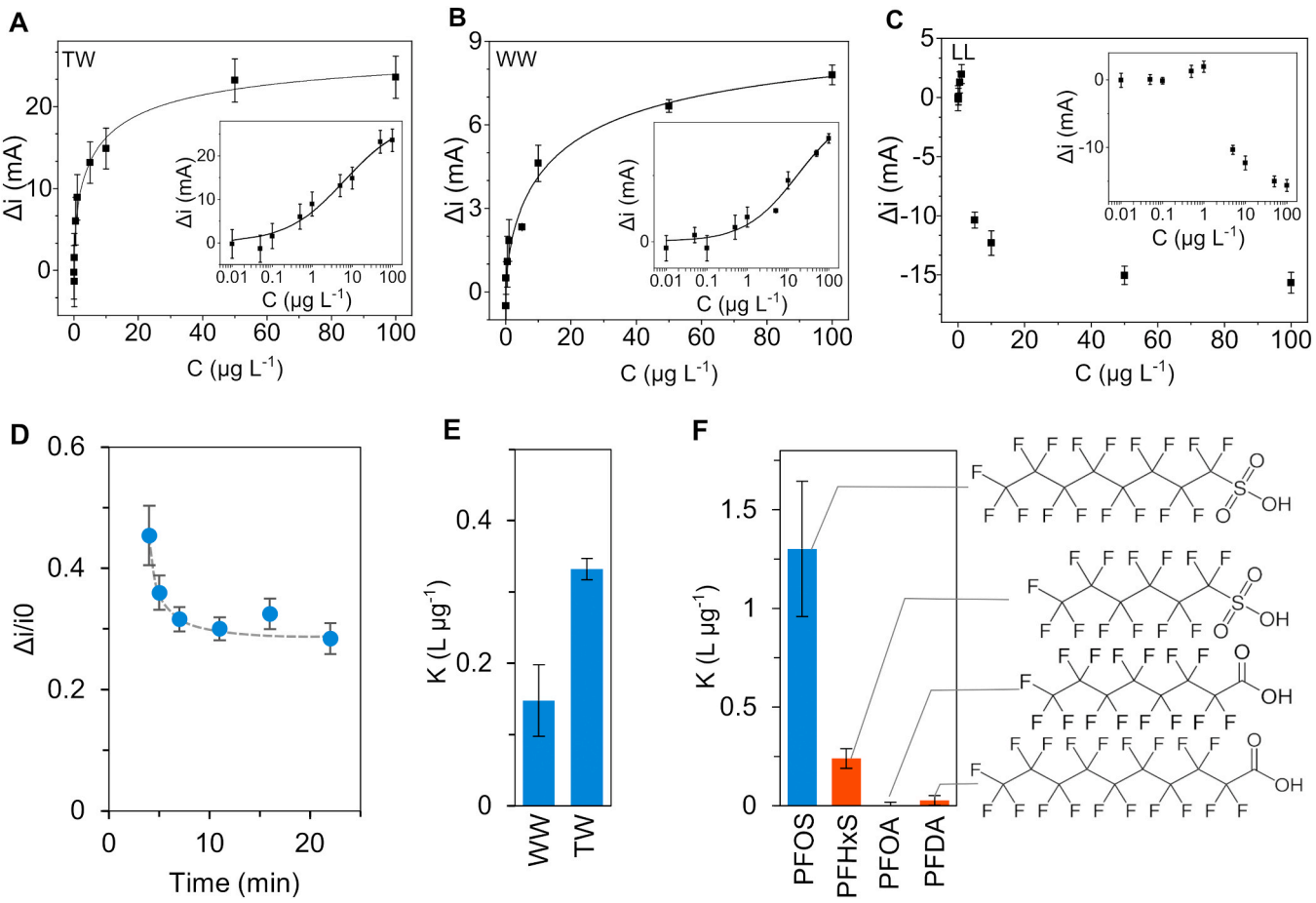

Fig. 7. Fitting of the (A-C) current differences with LF isotherm in real water matrices. (D) Effect of incubation time. Comparison of K among (E) different water matrices and (F) interferent species.

wider concentration ranges. On the other hand, a simple linear regression on the log-transformed concentrations provides a satisfactory PFOS quantification, only for a more limited range, at lower concentrations. It is also important to note that the obtained average recovery level (103 %) is in the range regarded as acceptable (70–110%) by the international bodies such as ISO, Eurachem, etc.

3.5. Selectivity, stability, repeatability of the CNW/eMIP sensor

The effect of the incubation time on the CNW/MIP response is shown in Fig. 7D. The selectivity of the MIP/CNW sensor was investigated by comparing the DPV and EIS responses to other PFAS with similar chemical structures (Fig. 7F). In particular, PFOA, PFOxS and PFDA were selected due to their similar chemical structures and the experimental data were fitted with an LF isotherm at equal molar

Table 3
Comparison of the MIP Analytical Techniques for the Detection of PFOS.

Electrode	Detection method	Range	LOD	Real sample	Pretreatment	Ref.
TiO_2-NT/MIP	Photoelectrochemical	Linear, 0.5–10 μM	86 μg L^{-1}	River, mountain and tap waters	0.22 μm filtration	Li et al.,[29]
GCE/MIP	DPV, EIS (fit)	Log, 0.05–0.5 nM	3.4 pM	River water	ns	Clark, Dick[9]
SiO_2-NPP/MIP	Fluorescence	Linear 5.57–48.54 μg L^{-1}	5.57 μg L^{-1}	River water	0.22 μm filtration	Moro et al.,[37]
Chitosan-CQDs	Fluorescence	Linear, 1–200 μg/L	0.66 (serum), 0.85 pg L^{-1} (urine)	Serum, urine	100-times dilution	Jiao et al.,[24]
Au/MIP	DPV	Linear 0.1–4.9 nM 9.5 nM – 1.5 μM	0.04 nM	Tap, distilled, bottled mineral waters	ns	Karimian et al., [25]
MIPPDA/AuNPs/ GCE	DPV	Linear, 0.01–8.00 μM	4.2 nM	water	ns	Gao et al.,[19]
CNW/MIP	DPV, EIS (fit + regression)	LF, 0.1–100 μg L^{-1}	1.2 μg L^{-1} (TW) 1.5 μg L^{-1} (WW)	Tap and wastewater	1:1 dilution	*This study*

*GCE: glassy carbon electrode, NT: nanotubes, NP: nanoparticles; ns: not specified
MIP-PR – molecularly imprinted phenolic resin
MIPPDA/AuNPs/GCE – molecularly imprinted polymer prepared through the in situ electropolymerisation of dopamine /gold nanoparticles (AuNPs) /glass carbon electrode (GCE)

MOST WIEDZY Downloaded from mostwiedzy.pl

concentrations. Instead of evaluating only the sensor response to PFOS in the presence of the interferents, a full binding isotherm (Fig. S8) of the synthesised CNW/MIP sensor was performed to directly compare the binding affinity of the three interferents. Furthermore, it is worth noting that the binding affinity in real media (TW and WW) is lower than that evaluated in PB, and in particular the K for TW is higher than for WW (Fig. 6E). Sensor reproducibility was assessed by measuring the basic parameters (e.g., electrical conductivity) and by Raman spectroscopy on samples synthesised from different PECVD processes and by comparison with our previous studies. Table 3 reports the comparison between the current and other literature studies.

4. Conclusions

Gaining insight into how the chemical and morphological characteristics of the substrate impact the electropolymerised MIP layer is essential for designing optimised recognition sites with specificity. In this study, we synthesised six different substrates using MPECVD, tailoring their electrical properties and surface features. This research represents a significant step forward in the development of a deployable sensor for the unattended detection of PFOS in tap water and wastewater, capable of meeting current concentration limits. However, the study also highlights the limitations of the sensor when dealing with more complex matrices such as landfill leachate.

Regarding the sp^2-C rich CNW substrate, the larger effective area for sorption (EASA), due to its higher structures, proves advantageous for the MIP layer. The unique labyrinthine porosity of the CNW layer does not affect the electropolymerisation process. Despite the considerable thickness (3.8 μm) of the thickest substrate, the coating process remains uniform, as demonstrated by the linear relationship between the current measured in the absence of PFOS and the current limit relative to the number of binding sites. Comparing the BDD substrate, it exhibits a higher LF (Langmuir-Freundlich) binding constant, but the smaller EASA results in a narrower variation interval of the electrochemical parameters (R_{ct} and *i*), leading to lower sensitivity. Furthermore, the LF PFOS binding constant is one order of magnitude higher than similar analytes, such as PFHxS, PFOA, and PFDA.

The study compares the faradaic and non-faradaic detection of PFAS, finding no significant advantages in terms of a lower limit of detection (LOD). Furthermore, the singular value decomposition-partial least squares (SVD-PLS) analysis proves useful both in obtaining a PFOS concentration directly from raw EIS data without the need for an equivalent electrical circuit (EEC) fit and in providing valuable insights into the detection mechanism. The peak frequencies most influenced by the PFOS concentration are around 20 Hz (corresponding to the influence of R_{ct}), slightly decreasing to 10 Hz for shorter CNW layers and below 1 Hz in the finite diffusion region. Due to the superior EASA and lower heterogeneity, the CNW/MIP sensor provides a wider sensing range and higher sensitivity by incorporating a larger number of binding sites.

Overall, the developed MIP demonstrates successful detection of PFOS in various real matrices, including tap water and treated wastewater, with a LOD of 100 ng L^{-1}. However, its performance is poor when dealing with 1:1 and 1:4 diluted landfill leachate, likely due to the complexity of the matrix, including sulphates and humic substances. Extended density-functional theory (DFT) calculations reveal that the MIP's binding to the electrode is stronger on the CNW substrate due to the formation of specific C-N bonds. This finding helps explain the higher homogeneity of the MIP on the CNW substrate. However, the binding of PFOS to the MIP is strongest on the BDD-adsorber MIP due to the more compact nature of the MIP layer and greater conformational freedom. This aligns with the higher binding affinity observed in the electrochemical experiments.

The findings obtained in this study highlight the future prospects of utilising enhanced MIP-supported diamond-rich carbon nano-architectures for monitoring water pollution, with a specific focus on emerging contaminants. The proposed design of the sensor shows great potential in the development of in situ monitoring devices for PFOS, capable of operating effectively under realistic environmental concentrations and conditions. Ultimately, this technological advancement is expected to enable faster and more efficient mitigation efforts in aquatic environments that are impacted by hazardous contaminants.

Environmental implication

Why the studied material should be considered 'hazardous material'.

Per- and polyfluoroalkyl substances are emerging contaminants of interest to JHM. Perfluorooctanesulfonic acid (PFOS), the target analyte of the current study, belongs to the above class.

How the work helps address environmental problems.

The development of novel, advanced materials and techniques for the ubiquitous detection and quantification of PFAS for in situ applications is a key priority, both in the recent European Water Quality Directive and in the WHO's Sustainable Development Goals. The current study comprises the synthesis and application of a novel electrochemical sensor for the detection and quantification of PFOS in tap water and wastewater, under relevant environmental concentrations and conditions. This will lead to potential in situ measurements of PFOS, resulting in faster and more-effective mitigation measures in aquatic environments.

CRediT authorship contribution statement

Mattia Pierpaoli: Conceptualization, Methodology, Investigation, Formal analysis, Writing - Original Draft, Visualization, **Małgorzata Szopińska:** Methodology, Investigation, Formal analysis, Writing - Original Draft, **Adrian Olejnik:** Methodology, Software, Writing - Original Draft, Visualization, **Jacek Ryl:** Validation, Data Curation, Writing - Review & Editing, **Sylwia Fudala-Ksiażek:** Formal analysis, Resources, **Aneta Łuczkiewicz:** Supervision, Writing - Review & Editing, **Robert Bogdanowicz:** Resources, Writing - Review & Editing.

Declaration of Competing Interest

The authors declare that they have no known competing financial interests or personal relationships that could have appeared to influence the work reported in this paper.

Data availability

Data will be made available on request.

Acknowledgements

Firstly, we would like to thank the Editor and all the 8 Reviewers for the fruitful remarks and to give us the possibility to improve our manuscript. Financial support of these studies from Gdańsk University of Technology under the Nobelium - 'Excellence Initiative - Research University' programme (M.P.) is gratefully acknowledged. This research was partially supported by The National Centre for Research and Development in the framework of the NOR/POLNOR/i-CLARE/0038/2019 project (R.B.).

Appendix A. Supporting information

Supplementary data associated with this article can be found in the online version at doi:10.1016/j.jhazmat.2023.131873.

References

[1] Acharya, U., Bober, P., Thottappali, M.A., Morávková, Z., Konefał, M., Pfleger, J., 2021. Synthesis and impedance spectroscopy of poly(P-phenylenediamine)/

MOST WIEDZY Downloaded from mostwiedzy.pl

montmorillonite composites. Polymers 13. https://doi.org/10.3390/polym13183132.
[2] Ansell, R.J., 2015. Characterization of the binding properties of molecularly imprinted polymers. Mol Impr Polym Biotechnol 51–93.
[3] Ayestarán Latorre, C., Ewen, J.P., Dini, D., Righi, M.C., 2021. Ab initio insights into the interaction mechanisms between boron, nitrogen and oxygen doped diamond surfaces and water molecules. Carbon 171, 575–584. https://doi.org/10.1016/j.carbon.2020.09.044.
[4] Beduk, T., Ait Lahcen, A., Tashkandi, N., Salama, K.N., 2020. One-step electrosynthesized molecularly imprinted polymer on laser scribed graphene bisphenol a sensor. Sens Actuators, B Chem 314, 128026. https://doi.org/10.1016/j.snb.2020.128026.
[5] Bogdanowicz, R., Ryl, J., 2022. Structural and electrochemical heterogeneities of boron-doped diamond surfaces. Curr Opin Electrochem 31, 100876. https://doi.org/10.1016/j.coelec.2021.100876.
[6] Brodowski, M., Pierpaoli, M., Janik, M., Kowalski, M., Ficek, M., Slepski, P., et al., 2022. Enhanced susceptibility of SARS-CoV-2 spike RBD protein assay targeted by cellular receptors ACE2 and CD147: multivariate data analysis of multisine impedimetric response. Sens Actuators B Chem 370, 132427. https://doi.org/10.1016/j.snb.2022.132427.
[7] Camurri, G., Ferrarini, P., Giovanardi, R., Benassi, R., Fontanesi, C., 2005. Modelling of the initial stages of the electropolymerization mechanism of o-phenylenediamine. J Electroanal Chem 585, 181–190.
[8] Chuiprasert, J., Srinives, S., Boontanon, N., Polprasert, C., Ramungul, N., Lertthanaphol, N., et al., 2022. Electrochemical sensor based on a composite of reduced graphene oxide and molecularly imprinted copolymer of polyaniline-poly (o-phenylenediamine) for ciprofloxacin determination: fabrication, characterization, and performance evaluation. ACS Omega. https://doi.org/10.1021/acsomega.2c07095.
[9] Clark, R.B., Dick, J.E., 2020. Electrochemical sensing of perfluorooctanesulfonate (PFOS) using ambient oxygen in river water. ACS Sens 5, 3591–3598. https://doi.org/10.1021/acssensors.0c01894.
[10] Cordner, A., Goldenman, G., Birnbaum, L.S., Brown, P., Miller, M.F., Mueller, R., Patton, S., Salvatore, D.H., Trasande, L., 2021. The True Cost of PFAS and the Benefits of Acting Now. https://doi.org/10.1021/acs.est.1c03565.
[11] Cowen, T., Karim, K., Piletsky, S., 2016. Computational approaches in the design of synthetic receptors – a review. Anal Chim Acta 936, 62–74. https://doi.org/10.1016/j.aca.2016.07.027.
[12] de Freitas Araújo, K.C., Vieira dos Santos, E., Pierpaoli, M., Ficek, M., Santos, J.E. L., Martínez-Huitle, C.A., et al., 2022. Diamondized carbon nanoarchitectures as electrocatalytic material for sulfate-based oxidizing species electrogeneration. Electrochim Acta 430, 1–11. https://doi.org/10.1016/j.electacta.2022.141069.
[13] Du, Z., Deng, S., Bei, Y., Huang, Q., Wang, B., Huang, J., et al., 2014. Adsorption behavior and mechanism of perfluorinated compounds on various adsorbents – a review. J Hazard Mater 274, 443–454. https://doi.org/10.1016/j.jhazmat.2014.04.038.
[14] EPA, 2022. Designation of Perfluorooctanoic Acid (PFOA) and Perfluorooctanesulfonic Acid (PFOS) as CERCLA Hazardous Substances [WWW Document]. URL ⟨https://www.govinfo.gov/content/pkg/FR-2022–09-06/pdf/2022–18657.pdf⟩.
[15] Espinoza, L.C., Aranda, M., Contreras, D., Henríquez, A., Salazar, R., 2019. Effect of the sp3/sp2 ratio in boron-doped diamond electrodes on the degradation pathway of aniline by anodic oxidation. ChemElectroChem 6, 4801–4810.
[16] Fernando, P.U.A.I., Glasscott, M.W., Kosgei, G.K., Cobb, J.S., Alberts, E.M., Bresnahan, C.G., et al., 2021. Toward rational design of electrogenerated molecularly imprinted polymers (eMIPs): maximizing monomer/template affinity. ACS Appl Polym Mater 3, 4523–4533. https://doi.org/10.1021/acsapm.1c00575.
[17] Fonseca, M.C., Nascimento, C.S., Borges, K.B., 2016. Theoretical investigation on functional monomer and solvent selection for molecular imprinting of tramadol. Chem Phys Lett 645, 174–179. https://doi.org/10.1016/j.cplett.2015.12.061.
[18] Fudala-Ksiazek, S., Pierpaoli, M., Kulbat, E., Luczkiewicz, A., 2016. A modern solid waste management strategy – the generation of new by-products. Waste Manag 49, 516–529. https://doi.org/10.1016/j.wasman.2016.01.022.
[19] Gao, Y., Gou, W., Zeng, W., Chen, W., Jiang, J., Lu, J., 2023. Determination of perfluorooctanesulfonic acid in water by polydopamine molecularly imprinted/gold nanoparticles sensor. Microchem J, 108378.
[20] Geladi, P., Nelson, A., Lindholm-Sethson, B., 2007. Complex numbers in chemometrics. Examples from multivariate impedance measurements on lipid monolayers. Anal Chim Acta 595, 152–159. https://doi.org/10.1016/j.aca.2007.01.037.
[21] Geladi, P., Sethson, B., Nyström, J., Lillhonga, T., Lestander, T., Burger, J., 2004. Chemometrics in spectroscopy: Part 2. Examples. Spectrochim Acta - Part B Spectrosc 59, 1347–1357. https://doi.org/10.1016/j.sab.2004.06.009.
[22] Guo, H., Liu, Y., Ma, W., Yan, L., Li, K., Lin, S., 2018. Surface molecular imprinting on carbon microspheres for fast and selective adsorption of perfluorooctane sulfonate. J Hazard Mater 348, 29–38. https://doi.org/10.1016/j.jhazmat.2018.01.018.
[23] Hirschorn, B., Orazem, M.E., Tribollet, B., Vivier, V., Frateur, I., Musiani, M., 2010. Determination of effective capacitance and film thickness from constant-phase-element parameters. Electrochim Acta 55, 6218–6227. https://doi.org/10.1016/j.electacta.2009.10.065.
[24] Jiao, Z., Li, J., Mo, L., Liang, J., Fan, H., 2018. A molecularly imprinted chitosan doped with carbon quantum dots for fluorometric determination of perfluorooctane sulfonate. Microchim Acta 185, 1–9. https://doi.org/10.1007/s00604-018-2996-y.
[25] Karimian, N., Stortini, A.M., Moretto, L.M., Costantino, C., Bogialli, S., Ugo, P., 2018. Electrochemosensor for trace analysis of perfluorooctanesulfonate in water based on a molecularly imprinted poly (o-phenylenediamine) polymer. ACS Sens 3, 1291–1298.
[26] Khan, M.S., Pal, S., Krupadam, R.J., 2015. Computational strategies for understanding the nature of interaction in dioxin imprinted nanoporous trappers. J Mol Recognit 28, 427–437.
[27] Ktari, N., Fourati, N., Zerrouki, C., Ruan, M., Seydou, M., Barbaut, F., et al., 2015. Design of a polypyrrole MIP-SAW sensor for selective detection of flumequine in aqueous media. Correlation between experimental results and DFT calculations. RSC Adv 5, 88666–88674. https://doi.org/10.1039/c5ra16237h.
[28] Kumar, R.S., Govindan, K., Ramakrishnan, S., Kim, A.R., Kim, J.-S., Yoo, D.J., 2021. Fe3O4 nanorods decorated on polypyrrole/reduced graphene oxide for electrochemical detection of dopamine and photocatalytic degradation of acetaminophen. Appl Surf Sci 556, 149765.
[29] Li, J., Feng, H., Cai, J., Yuan, L., Wang, N., Cai, Q., 2014. Molecularly imprinted polymer modified TiO2 nanotube arrays for photoelectrochemical determination of perfluorooctane sulfonate (PFOS). Sens Actuators B Chem 190, 745–751.
[30] Li, X., He, Y., Zhao, F., Zhang, W., Ye, Z., 2015. Molecularly imprinted polymer-based sensors for atrazine detection by electropolymerization of o-phenylenediamine. RSC Adv 5, 56534–56540.
[31] Losito, I., Palmisano, F., Zambonin, P.G., 2003. o-Phenylenediamine electropolymerization by cyclic voltammetry combined with electrospray ionization-ion trap mass spectrometry. Anal Chem 75, 4988–4995.
[32] Luise, D., d'Alterio, M.C., Talarico, G., Ciofini, I., Labat, F., 2022. Modeling the spectral properties of poly (x-phenylenediamine) conducting polymers using a combined TD-DFT and electrostatic embedding approach. J Comput Chem 43, 2001–2008.
[33] Luliński, P., Sobiech, M., Żołek, T., Maciejewska, D., 2014. A separation of tyramine on a 2-(4-methoxyphenyl) ethylamine imprinted polymer: an answer from theoretical and experimental studies. Talanta 129, 155–164.
[34] Luo, D., Zhao, Z., Zhang, L., Wang, Q., Wang, J., 2014. On the structure of molecularly imprinted polymers by modifying charge on functional groups through molecular dynamics simulations. Mol Simul 40, 431–438.
[35] Ma, P., Yang, W., Fan, T., Liu, H., Zhou, Z., Li, J., et al., 2015. Surface imprinted polymers for oil denitrification with the combination of computational simulation and multi-template molecular imprinting. Polym Adv Technol 26, 476–486.
[36] Monti, S., Cappelli, C., Bronco, S., Giusti, P., Ciardelli, G., 2006. Towards the design of highly selective recognition sites into molecular imprinting polymers: a computational approach. Biosens Bioelectron 22, 153–163.
[37] Moro, G., Cristofori, D., Bottari, F., Cattaruzza, E., De Wael, K., Moretto, L.M., 2019. Redesigning an electrochemical MIP sensor for PFOS: practicalities and pitfalls. Sensors 19. https://doi.org/10.3390/s19204433.
[38] Niedzialkowski, P., Koterwa, A., Olejnik, A., Zielinski, A., Gornicka, K., Brodowski, M., et al., 2022. Deciphering the molecular mechanism of substrate-induced assembly of gold nanocube arrays toward an accelerated electrocatalytic effect employing heterogeneous diffusion field confinement. Langmuir 38, 9597–9610.
[39] Ostovan, A., Arabi, M., Wang, Y., Li, J., Li, B., Wang, X., et al., 2022. Greenificated molecularly imprinted materials for advanced applications. Adv Mater 34, 1–32. https://doi.org/10.1002/adma.202203154.
[40] Oyama, N., Ohsaka, T., Chiba, K., Takahashi, K., 1988. Effects of supporting electrolyte and pH on charge transport within electropolymerized poly(o -phenylenediamine) films deposited on graphite electrodes. Bull Chem Soc Jpn 61, 1095–1101. https://doi.org/10.1246/bcsj.61.1095.
[41] Pacheco, J.G., Castro, M., Machado, S., Barroso, M.F., Nouws, H.P.A., Delerue-Matos, C., 2015. Molecularly imprinted electrochemical sensor for ochratoxin A detection in food samples. Sens Actuators, B Chem 215, 107–112. https://doi.org/10.1016/j.snb.2015.03.046.
[42] Pierpaoli, M., Ficek, M., Jakobczyk, P., Karczewski, J., Bogdanowicz, R., 2021. Self-assembly of vertically oriented graphene nanostructures: multivariate characterisation by Minkowski functionals and fractal geometry. Acta Mater, 116989. https://doi.org/10.1016/j.actamat.2021.116989.
[43] Pierpaoli, M., Ficek, M., Rycewicz, M., Sawczak, M., Karczewski, J., Ruello, M., et al., 2019. Tailoring electro/optical properties of transparent boron-doped carbon nanowalls grown on quartz. Materials 12, 547. https://doi.org/10.3390/ma12030547.
[44] Pierpaoli, M., Jakobczyk, P., Sawczak, M., Łuczkiewicz, A., Fudala-Książek, S., Bogdanowicz, R., 2021. Carbon nanoarchitectures as high-performance electrodes for the electrochemical oxidation of landfill leachate. J Hazard Mater 401, 123407. https://doi.org/10.1016/j.jhazmat.2020.123407.
[45] Pierpaoli, M., Lewkowicz, A., Dec, B., Nadolska, M., Bogdanowicz, R., 2022. Impedimetric sensing of α-amino acids driven by micro-patterned 1,8-Diazafluoren-9-one into titania- boron- doped maze-like nanocarbons. Sens Actuators B Chem 371. https://doi.org/10.1016/j.snb.2022.132459.
[46] Pierpaoli, M., Szopińska, M., Wilk, B.K., Sobaszek, M., Łuczkiewicz, A., Bogdanowicz, R., et al., 2021. Electrochemical oxidation of PFOA and PFOS in landfill leachates at low and highly boron-doped diamond electrodes. J Hazard Mater 403. https://doi.org/10.1016/j.jhazmat.2020.123606.
[47] R Core Team, 2013. R: A language and environment for statistical computing.
[48] Ratautaite, V., Nesladek, M., Ramanaviciene, A., Baleviciute, I., Ramanavicius, A., 2014. Evaluation of histamine imprinted polypyrrole deposited on boron doped nanocrystalline diamond. Electroanalysis 26, 2458–2464. https://doi.org/10.1002/elan.201400294.
[49] Rodrigues, D.R., Olivieri, A.C., Fragoso, W.D., Lemos, S.G., 2019. Complex numbers-partial least-squares applied to the treatment of electrochemical

MOST WIEDZY Downloaded from mostwiedzy.pl

impedance spectroscopy data. Anal Chim Acta 1080, 1–11. https://doi.org/10.1016/j.aca.2019.07.047.
[50] Sayyah, S.M., El-Deeb, M.M., Kamal, S.M., Azooz, R.E., 2009. Electropolymerization of o-phenylenediamine on Pt-electrode from aqueous acidic solution: kinetic, mechanism, electrochemical studies and characterization of the polymer obtained. J Appl Polym Sci 112, 3695–3706.
[51] Schauperl, M., Lewis, D.W., 2015. Probing the structural and binding mechanism heterogeneity of molecularly imprinted polymers. J Phys Chem B 119, 563–571.
[52] Sestrem, R.H., Ferreira, D.C., Landers, R., Temperini, M.L.A., do Nascimento, G.M., 2010. Synthesis and spectroscopic characterization of polymer and oligomers of ortho-phenylenediamine. Eur Polym J 46, 484–493.
[53] Sharma, P.S., Garcia-Cruz, A., Cieplak, M., Noworyta, K.R., Kutner, W., 2019. 'Gate effect' in molecularly imprinted polymers: the current state of understanding. Curr Opin Electrochem 16, 50–56. https://doi.org/10.1016/j.coelec.2019.04.020.
[54] Sobiech, M., Żołek, T., Luliński, P., Maciejewska, D., 2014. A computational exploration of imprinted polymer affinity based on voriconazole metabolites. Analyst 139, 1779–1788. https://doi.org/10.1039/c3an01721d.
[55] Söderholm, S., Roos, Y.H., Meinander, N., Steinby, K., 2000. Theoretical and experimental vibrational study of polyaniline in base forms: non-planar analysis. Part I. J Raman Spectrosc 31, 1029–1039. https://doi.org/10.1002/1097-4555(200011)31:11<1029::AID-JRS640>3.0.CO;2-A.
[56] Soler, J.M., Artacho, E., Gale, J.D., García, A., Junquera, J., Ordejón, P., et al., 2002. The SIESTA method for ab initio order-N materials simulation. J Phys Condens Matter 14, 2745.
[57] Song, J., Huang, M., Jiang, N., Zheng, S., Mu, T., Meng, L., et al., 2020. Ultrasensitive detection of amoxicillin by TiO2-g-C3N4@ AuNPs impedimetric aptasensor: fabrication, optimization, and mechanism. J Hazard Mater 391, 122024.
[58] The European Parliament and the Council of the European Union, 2020. Directive (EU) 2020/2184 of the European parliament and of the council. J Eur Union 2019, 1–62.
[59] Troullier, N., Martins, J.L., 1991. Efficient pseudopotentials for plane-wave calculations. Phys Rev B 43, 1993.
[60] Ullah, H., Shah, A.-H.A., Ayub, K., Bilal, S., 2013. Density functional theory study of poly (o-phenylenediamine) oligomers. J Phys Chem C 117, 4069–4078.
[61] Umpleby, R.J., Baxter, S.C., Rampey, A.M., Rushton, G.T., Chen, Y., Shimizu, K.D., 2004. Characterization of the heterogeneous binding site affinity distributions in molecularly imprinted polymers. J Chromatogr B Anal Technol Biomed Life Sci 804, 141–149. https://doi.org/10.1016/j.jchromb.2004.01.064.
[62] Wang, L., Yu, J., Wang, X., Li, J., Chen, L., 2023. Molecular imprinting-based nanocomposite adsorbents for typical pollutants removal. J Hazard Mater Lett 4, 100073. https://doi.org/10.1016/j.hazl.2022.100073.
[63] Yola, M.L., Atar, N., 2019. Development of molecular imprinted sensor including graphitic carbon nitride/N-doped carbon dots composite for novel recognition of epinephrine. Compos Part B Eng 175, 107113. https://doi.org/10.1016/j.compositesb.2019.107113.
[64] Zhang, H.P., Luo, J., Huang, H.G., Wu, L.L., Lin, Z.H., 2000. Electrochemical assembly of nano-organized poly-o-phenylenediamine films. Chem Phys Lett 326, 169–174. https://doi.org/10.1016/S0009-2614(00)00747-8.
[65] Zhang, X., Li, G., Wang, J., Chu, J., Wang, F., Hu, Z., et al., 2022. Revisiting the structure and electrochemical performance of poly (o-phenylenediamine) as an organic cathode material. ACS Appl Mater Interfaces 14, 27968–27978.

MOST WIEDZY Downloaded from mostwiedzy.pl